Manipulating Spin Chirality of Magnetic Skyrmion Bubbles by In-Plane Reversed Magnetic Fields in $(Mn_{1-x}Ni_x)_{65}Ga_{35}$ ($x = 0.45$) Magnet

Bei Ding,[1,2] Jie Cui,[1,2] Guizhou Xu,[3] Zhipeng Hou,[1] Hang Li,[1,2] Enke Liu,[1] Guangheng Wu,[1] Yuan Yao,[1,*] and Wenhong Wang[1,4,†]

[1] *Beijing National Laboratory for Condensed Matter Physics and Institute of Physics, Chinese Academy of Sciences, Beijing 100190, China*

[2] *University of Chinese Academy of Sciences, Beijing 100049, China*

[3] *School of Materials Science and Engineering, Nanjing University of Science and Technology, Nanjing 210094, China*

[4] *Songshan Lake Materials Laboratory, Dongguan, Guangdong 523808, China*

(Received 10 July 2019; revised manuscript received 23 September 2019; published 26 November 2019)

Understanding the dynamics of the magnetic skyrmion, a particlelike topologically stable spin texture, and its response dynamics to external fields are indispensable for applications in spintronic devices. Here, Lorentz transmission electron microscopy is used to investigate the spin chirality of magnetic skyrmion bubbles (SKBs) in the centrosymmetric magnet $(Mn_{1-x}Ni_x)_{65}Ga_{35}$ at room temperature. The reversal of SKBs excited by the in-plane magnetic field is revealed. Moreover, the collective behavior of interacting spin chirality can be manipulated by reversing the directions of the magnetic fields on a wedge-shaped thin plate. The dynamic behavior of bubbles at different positions on the thin plate is explored through micromagnetic simulation, which indicates a nonuniform and nontrivial dynamic magnetization on the surfaces and center of the thin plate during spin chirality reversal. The results suggest that the controllable symmetry breaking of the SKBs, arising from thickness variation, provides the ability to manipulate the collective behavior of the spin chirality with small external fields, leading to a promising application in nonvolatile spintronic devices for magnetic skyrmions.

DOI: 10.1103/PhysRevApplied.12.054060

I. INTRODUCTION

Skyrmions, particlelike topologically stable spin textures, are usually stabilized by the Dzyaloshinskii-Moriya interaction (DMI) in noncentrosymmetric magnets with broken inversion symmetry, such as Mn-Si [1–3], Fe-Ge [4,5], Fe-Co-Si [6], Cu_2OSeO_3 [7–9], and Mn-Pt-Sn [10]. The response dynamics of magnetic skyrmions to external stimuli is an important property for the manipulation of skyrmions that is indispensable for practical applications in spintronics. The stability of skyrmions is investigated by using various external stimuli, including electromagnetic wave resonance [11], cooling [12], anisotropic mechanical strain [13], and an electric field [14,15]. Moreover, control of skyrmions' chirality is demonstrated by means of the chemical composition [16], grain orientation [5,17], and in-plane magnetic field [18]. Similar behavior is expected for other topologically nontrivial spin textures known as magnetic skyrmion bubbles (SKBs) in some centrosymmetric magnets with dipole-dipole interactions and uniaxial magnetic anisotropy, such as Mn-Ni-Ga [19], Ni_2MnGa [20], Fe_3Sn_2 [21], and $Ba(Fe_{1-x-0.05}Sc_xMg_{0.05})_{12}O_{19.16}$ [22]. Contrary to DMI-stabilized skyrmions with a fixed chirality, SKBs in centrosymmetric magnets possess two degrees of freedom, i.e., vorticity and helicity [23], which makes them suitable for manipulating spin chirality and topological textures through stimuli.

Recent simulations demonstrate that the chirality reversal of SKBs can be controlled by tuning the driving current density [24], which allows potential application as a binary memory device. In addition, thermal activation can also reverse the SKB's helicity [25], although it is not suitable for practical applications. Yu *et al.* [22,26] found that chirality reversal occurred while tilting the applied magnetic field, but the demand for out-of-plane bias or low temperature limited its realization in future devices. Furthermore, field-free biskyrmion bubbles have been explored in centrosymmetric hexagonal Mn-Ni-Ga alloys at room temperature via an appropriate field cooling (FC) procedure [19,27]. Here, motivated by the abovementioned approaches, manipulation of the spin chirality of the field-free skyrmion bubble lattice (SKBL) generated

*yaoyuan@iphy.ac.cn
†wenhong.wang@iphy.ac.cn

within a wedge-shaped $(Mn_{1-x}Ni_x)_{65}Ga_{35}$ ($x = 0.45$) thin plate is demonstrated by in situ Lorentz transmission electron microscopy (LTEM) with the help of an in-plane magnetic field at room temperature. Micromagnetic simulation reproduces the collective reversal behavior of the SKB chirality. Moreover, the dynamic transitions at different positions on the thin plate are investigated, indicating nonuniform and nontrivial dynamic magnetization on the surfaces and center of the thin plate during spin chirality reversal.

II. METHODS

A. Sample preparation

Experiments are performed on a polycrystalline $(Mn_{1-x}Ni_x)_{65}Ga_{35}$ ($x = 0.45$) sample, which is synthesized by arc-melting mixtures of high purity Mn, Ni, and Ga in a pure argon atmosphere. The crystal structure of the alloy is studied using powder x-ray diffraction measurements, which demonstrate a hexagonal structure with a space group of $P6_3/mmc$ (No. 194) [Fig. 1(a)]. The Curie temperature, T_C, is determined to be 345 K from the temperature dependence of magnetization. The singular point detection (SPD) technique [28–30] is applied to calculate the anisotropy of the oriented polycrystalline $(Mn_{1-x}Ni_x)_{65}Ga_{35}$ ($x = 0.45$) samples. The hysteresis loops are measured under a series of the field (50 Oe, 100 Oe, 150 Oe, and 200 Oe) with the bulk sample reflecting a weak coercivity (see Fig. S1 within the Supplemental Material [31]).

B. Sample thickness measurements

The thin plate for LTEM observation is cut from the polycrystalline bulk and thinned by means of mechanical polishing and argon-ion milling, which results in a wedgelike variation in thickness (see Fig. S2 within the Supplemental Material [31]). The thickness of the sample region is measured by using electron energy-loss spectroscopy (EELS) log-ratio techniques with a Titan G2 60–300 microscope (FEI). The normalized thickness (t/λ; t represents thickness, λ indicates the free path for inelastic scattering of the electron beam in the material) map is, together with a series of EELS spectra, extracted from the spectrum image. By taking account of the spectrum collection conditions ($E_0 = 300$ kV, $\alpha = 24$ mrad, $\beta = 8.6$ mrad),

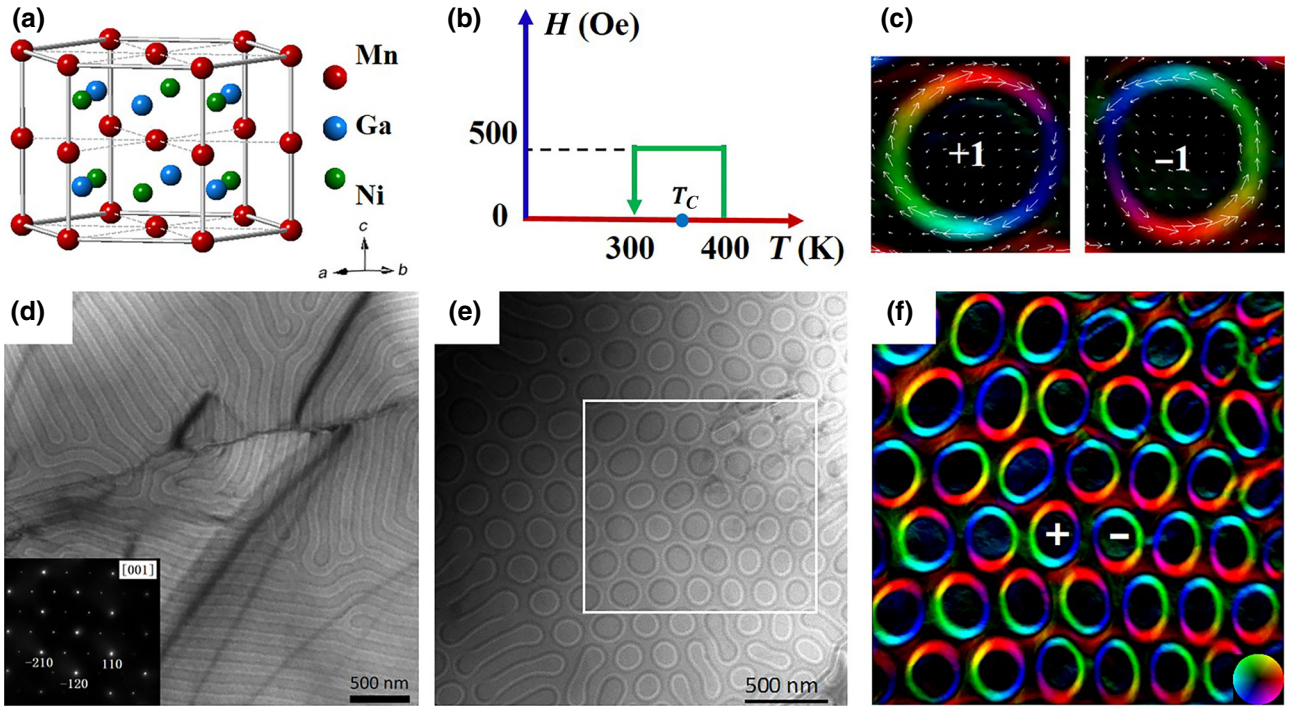

FIG. 1. Structure and magnetic domain textures observed in the $(Mn_{1-x}Ni_x)_{65}Ga_{35}$ thin plate with $x = 0.45$. (a) Schematic crystal structures of a layered Ni_2In-type structure Mn-Ni-Ga, with alternating stacks of Mn atomic layers and Ni-Ga atomic layers along the c axis. (b) Schematic illustration of the FC procedure. (d) Magnetic stripe domain textures observed at room temperature along the [001] axis. The inset shows the selected area electron diffraction pattern (SEAD) for a single-crystalline domain. (e) Real-space observation of zero-magnetic-field room-temperature skyrmion bubbles ($C = \pm 1$) and magnetic stripe after FC manipulation. (f) In-plane magnetization of selected skyrmion bubbles from (e). (c) Magnified images of two skyrmion bubbles with opposite chirality indicated in (f). Color wheel and arrows indicate the magnitude and direction of the in-plane magnetization. "+" and "−" represent the clockwise ($C = 1$) and counterclockwise ($C = -1$) chirality of the skyrmion bubbles.

the inelastic mean free paths, λ, of the sample are calculated.

C. LTEM measurements

Magnetic domain contrast is made by using a Titan G2 60–300 instrument in LTEM mode equipped with a double-tilt heating holder and a JEOL 2100F Lorentz transmission electron microscope equipped with a magnetic field holder. To obtain a zero free SKBL, a double-tilt heating holder (Model 652, Gatan Inc.) with a smart hot stage controller (Model 901, Gatan Inc.) is used to raise the specimen temperature from 300 to 400 K. The specific FC manipulation is as follows. First, the sample is heated to 360 K, which is higher than that of the Curie temperature, $T_C \sim 345$ K. Second, a small perpendicular magnetic field of 500 Oe is applied by increasing the objective lens current gradually in very small increments. Third, the temperature of the sample is cooled gradually from 360 to 300 K. Finally, at 300 K, the small perpendicular magnetic field is turned off. The experimental process is recorded by a charge-coupled device (CCD) camera (see Video 1 within the Supplemental Material [31]). A FC procedure here is needed only for the thin plate to generate the SKBs, but does not affect the subsequent manipulation of spin chirality of magnetic SKBs by reversing in-plane magnetic fields (see Fig. S3 within the Supplemental Material [31]).

The in-plane magnetic field applied to switch the chirality of the SKBL is induced by the excitation coil in the magnetic field holder. To determine the chirality of SKBs, three sets of images (under-, over-, and in-focus) are acquired by using a CCD camera, and the in-plane magnetization distribution is obtained by using the QPT software based on the transport-of-intensity equation (TIE) [32].

D. Micromagnetic simulations

The micromagnetic simulations are carried out by using the 3D object-oriented micromagnetic framework (OOMMF) code [33]. Magnetization obtained from the OOMMF simulation is input into a homemade DIGITALMICROGRAPH script to simulate the LTEM images [34] (see Fig. S4 within the Supplemental Material [31]). The material parameters obtained from the experiments on $(Mn_{1-x}Ni_x)_{65}Ga_{35}$ ($x = 0.45$) are as follows: the saturation magnetization is $M_s = 8 \times 10^5$ A/m^3 and the magnetocrystalline anisotropy constant is $K_u = 2.65 \times 10^5$ J/m^3, which is measured by means of the SPD technique. The exchange constant, $A = 1.4 \times 10^{-11}$ J/m, and $D = \pi\sqrt{A/K_u}$, where D is the domain wall width, are obtained from the LTEM results.

First, for the analysis of skyrmion bubble chirality reversal dynamics, only a single skyrmion bubble is defined with a cylindrical geometry with experimentally observed structures. Slab geometries of dimensions 192 nm × 192 nm × (120–130 nm) are discretized with 1.5 nm tetrahedra. The magnetic field is applied along the x direction to transform the SKB into an achiral bubble. Then, the SKBL is simulated by using a slab with a volume of 1 μm × 1 μm × 100 nm and a wedge thickness varied from 100 to 130 nm with $6 \times 6 \times 2$ nm^3 mesh cell size. The quantity of $C = +1$ and $C = -1$ SKB dependences of the applied in-plane magnetic field times are investigated when in plane along the x or y directions of the SKBL.

III. RESULT AND DISSCUSSION

Various magnetic domains are observed on the wedge-shaped alloy specimen [35]; here, we focus only on the magnetic stripes along the [001] axis, as shown in Fig. 1(d). Based on previous work, a FC procedure [see Fig. 1(b)] is applied on the thin plate to generate the SKBL [27]. Figure 1(e) represents an overfocus LTEM image of the SKBL at room temperature and zero magnetic field, which coexists with the stripe domains. To characterize the in-plane topological magnetization texture in detail, we analyze the selected SKBL LTEM images by using the TIE technique [Fig. 1(f)]. The magnified topological textures in Fig. 1(c) clearly indicate two SKBs with opposite chirality. Accordingly, the dark and white SKBs shown in Fig. 1(e) can be denoted as clockwise "+" and anticlockwise "−," respectively. In addition, the achiral bubbles are observed in subsequent work (see Fig. 2) and corresponding magnetizations are shown in Fig. S4 within the Supplemental Material [31]. A chirality C is used to clarify these different bubbles: chiral bubbles with in-plane magnetization rotate either clockwise ($C = +1$) or counterclockwise ($C = -1$), while topological achiral bubbles have $C = 0$.

Figures 2(a)–2(i) illuminate the chirality switching of SKBs in a magnetic field parallel to the surface of the thin plate. The direction of the in-plane magnetic field is marked by the green arrow with a white rim. With an enhanced magnetic field, the SKBs with $C = \pm 1$ are converted into achiral bubbles ($C = 0$), as shown in Fig. 2(b). When the magnetic field decreases to zero, the achiral bubbles transform back into chiral SKBs [Fig. 2(c)]. This can be attributed to the fact that the energy of the SKBs is lower compared with that of the achiral bubbles [24]. As the field direction is reversed, the achiral bubbles appear again [Fig. 1(d)]. Fading of the field to zero leads to the recovery of chiral SKBs [Fig. 1(e)]. This process can be cycled reversibly many times [Figs. 2(a)–(i)].

With the intention of clearly analyzing the quantity of reversed SKBs, in Fig. 3(a) 37 SKBs are tracked. Figure 3(b) illustrates the variation of eight SKBs under different external fields, where each bubble displays a random reversal behavior. However, the statistical chirality of the SKBs discloses a collective effect if the in-plane magnetic field varies [Fig. 3(c)]. When a negative

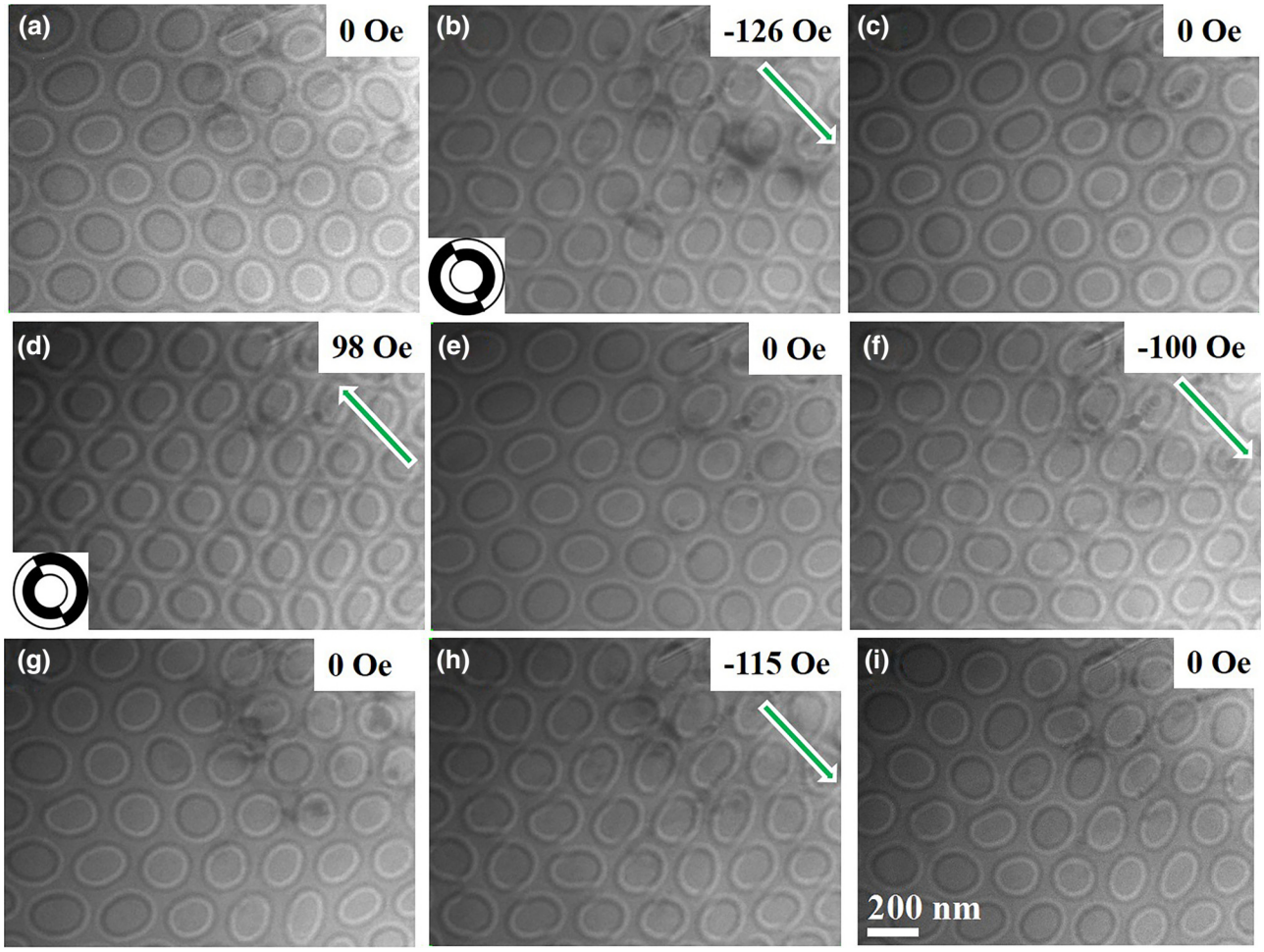

FIG. 2. Real-space observation of chirality transformation between skyrmion bubbles ($C = \pm 1$) and achiral bubbles ($C = 0$) induced by the applied in-plane magnetic field. (a)–(i) Bubbles observed at room temperature with various in-plane magnetic fields. The insets in (b),(d) show two kinds of achiral bubbles with opposite in-plane magnetic fields. The green arrow with a white rim indicates the direction of the in-plane magnetic field.

field is applied and reduced to zero, more $C = -1$ SKBs are formed. Upon reversing the field direction, $C = +1$ SKBs prefer to exist. Further investigations of another 86 SKBs with more switching processes are shown in Figs. 3(d)–3(f). These analyses qualitatively confirm that the statistical chirality cannot be reversed if the external in-plane field varies only in one direction, regardless of whether the strength of the field is large or small.

The modeling and simulation of the chirality reversal of the SKB after applying an in-plane magnetic field is discussed. Considering that the chirality preference mainly occurs upon fading of the in-plane magnetic field, we perform OOMMF simulations to systematically explore the mechanism behind the statistical chiral reversal of the SKB in a wedge-shaped slab after removal of the in-plane magnetic field [Fig. (4)]. The achiral bubble ($C = 0$) emerges when the SKB is stimulated by a higher in-plane magnetic field, as shown in Fig. 4(a). The magnetic spins reveal the twisting Néel domains, with counterswirling at the upper and bottom surfaces of the bubble. Inside of the cylindrical feature, the magnetic spins rearrange themselves to form two Bloch arches. Such variation of the magnetic spins results in location distortion of the cores along the axis, as demonstrated in the projection image in Fig. 4(a). As the in-plane magnetic field decreases, the magnetic spins at the top and bottom surface maintain the twisting features, but some inner magnetic spins begin to change their directions [Fig. (4b)]. The spins in the thinner part attenuate their M_x component, but the magnetization in the thicker part retains the initial direction due to different static magnetic energies related with the thickness, as demonstrated by further experimental analysis (see Fig. S5 within the Supplemental Material [31]). Meanwhile, the cores exhibit clockwise rotation at the weakened magnetic field, which is analogous to the SKB chirality. When the in-plane magnetic field disappears, the spins in the thinner part reverse completely and lead only to the energetically favorable $C = +1$ SKB, while the magnetic spins at the top and

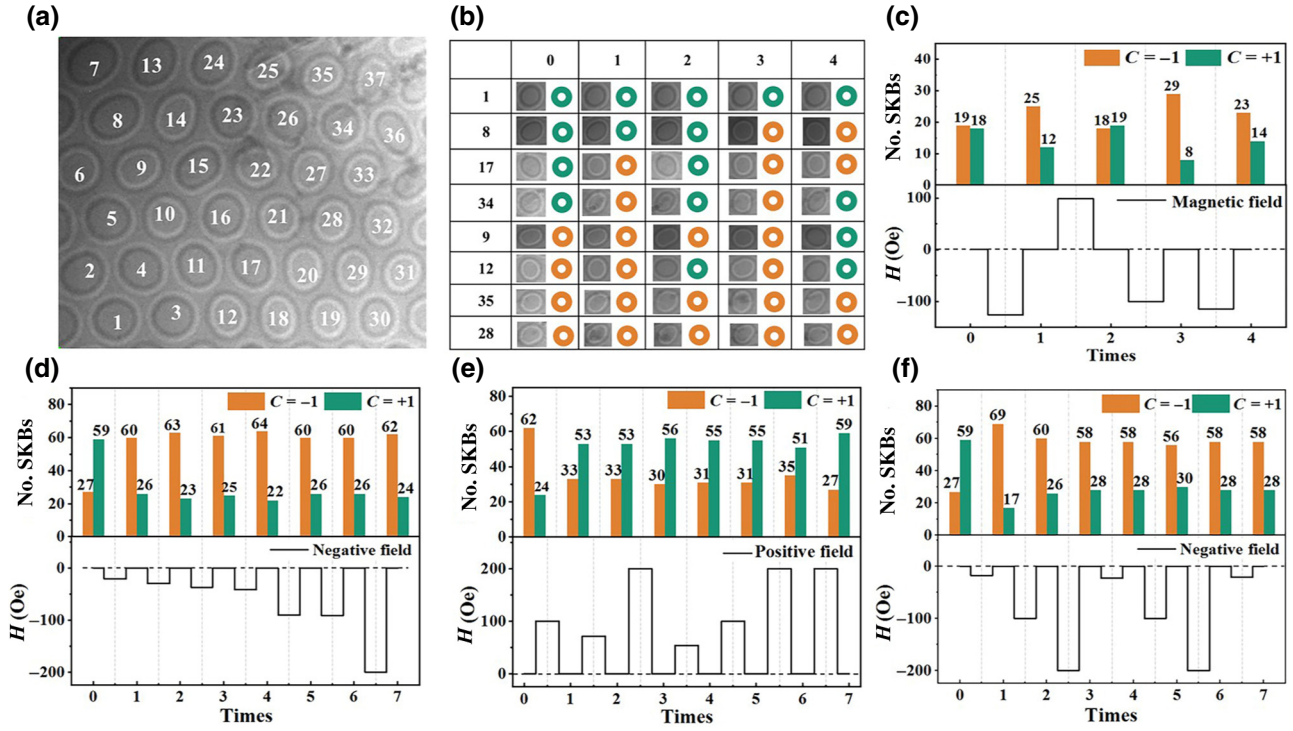

FIG. 3. Statistics of chirality reversal obtained after applying an in-plane field. (a) LTEM image obtained at room temperature under zero magnetic field is considered as the initial state. (b) The chirality reversal of some SKBs under different field conditions. Numbers in the first column are the labels of bubbles in (a), and numbers in the first row represent the corresponding magnetic field conditions in (c). The green and orange circles indicate clockwise ($C=+1$) and counterclockwise ($C=-1$) chirality of the skyrmion bubbles, respectively. (c) The upper histogram shows the statistical number of $C=\pm1$ skyrmion bubbles after application of the in-plane magnetic field. The orange and green bands indicate the numbers of $C=+1$ and $C=-1$ skyrmion bubbles, respectively. The corresponding number represents the value of $C=+1$ and $C=-1$ skyrmion bubbles. The lower chart is the applied magnetic field. (d–f) The statistics of $C=\pm1$ skyrmion bubbles after only applied positive or negative magnetic field, respectively.

bottom still retain the Néel twisting. At the same time, the cores return to the cylinder axis [Fig. 4(c)].

Some characteristics of single SKB chirality reversal are summarized below. First, the magnetization cores at different positions of the bubble axis form a swirl, which keeps pace with the SKB chirality during chirality recovery. Second, the chirality transition mainly occurs inside the bubble, despite the Néel twisting at both surfaces. This behavior can be explained from the perspective of energy. The total energy of a given system contains the exchange energy, the anisotropy energy, the Zeeman energy, and the demagnetization energy, which are shown in Fig. S6 within the Supplemental Material [31]. As the in-plane magnetic field varies, the demagnetizing field prefers to align the magnetic spins in plane, whereas the exchange interaction favors the magnetic spins aligning with each other. As a result, the magnetic spins at the surfaces are extremely hard to reverse; as for the interior, the magnetic spins are mainly affected by the Zeeman field, which forces the magnetization along the external field direction. However, this Néel twisting cannot be observed in the LTEM images because the image contrast is dominated chiefly by the inner magnetization, owing to the projection characteristic of the imaging process (see Fig. S7 within the Supplemental Material [31]). Third, the chirality preference arises from the thickness variation in the wedgelike sample. The spins in the thinner part change their orientation easily compared with the thicker part, when the external field decreases, which further determines the chirality of the SKB.

As observed in the experiment, here, we further perform a micromagnetic simulation of the SKBL with a wedge-shaped slab under a combination of in-plane magnetic fields. The simulation manifests some complexity. The schematic field-dependent evolution of SKBs ($C=\pm1$) and achiral bubbles ($C=0$) in a wedge-shaped slab is shown in Fig. 5(a), where B_0 is the critical field to degenerate the chiral or achiral states of a single bubble. First, a large negative in-plane field (along the $-x$ direction) perpendicular to the thickness gradient transforms the SKBs into achiral bubbles. As the field decreases, the achiral bubbles change into the $C=-1$ SKBs, following the above-described transition. If B fades from the positive direction, the procedure is inversed and the $C=+1$ SKBs

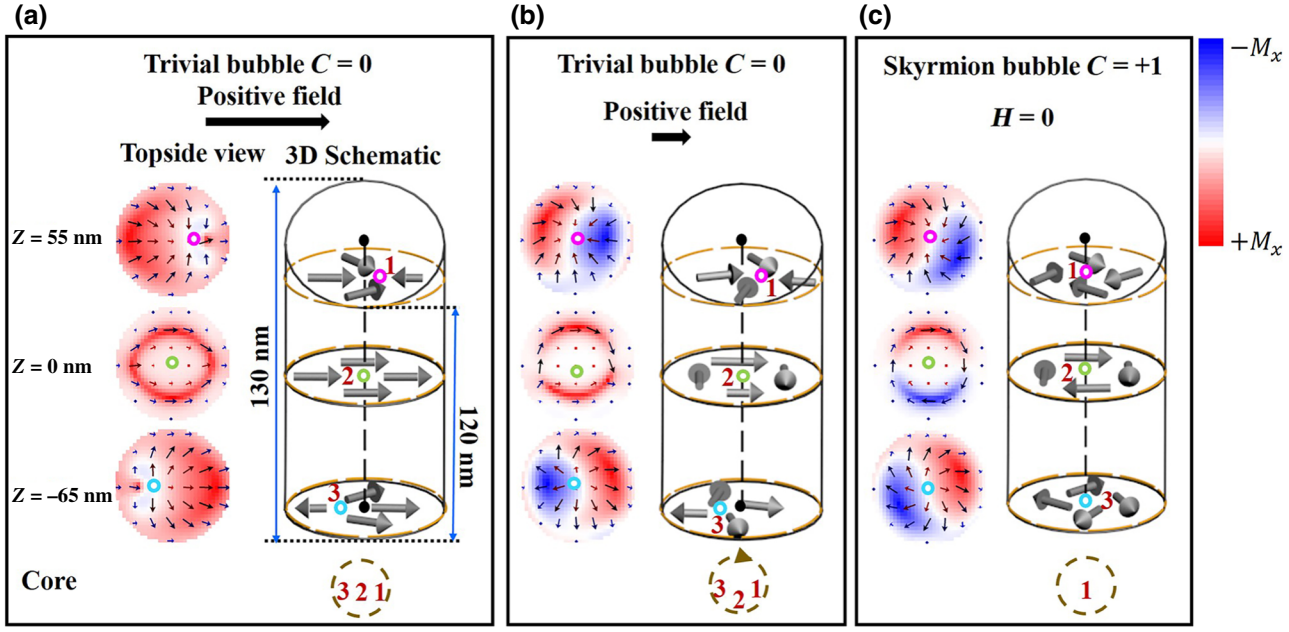

FIG. 4. (a)–(c) Micromagnetic structures of magnetization at different in-plane magnetic fields on a wedge-shaped plate, where the thinner edge faces the reader. The domain state is obtained from micromagnetic simulations. (a) The left column shows the topside views of the in-plane magnetization of the skyrmion bubble, with an arrow indicating the orientation and colorized M_x strength at three depth positions ($Z = 55$ nm, 0 nm, -65 nm). The locations of the magnetization cores at different depths are denoted by purple (1), green (2), and blue (3) circles in the 3D schematic bubble. The dotted line is the cylinder axis. The projection of the cores in different x-y planes is drawn below the cylinder. (b),(c) The redistribution of magnetization is detailed at the transformation process after removing the in-plane magnetic field.

are more favorable. Figure 5(b) displays the statistical distribution of the simulated SKBL, which is consistent with the experimental results in Figs. 3(d)–3(f). In principle, the chirality of the SKBs can be totally controlled by changing the direction of the in-plane magnetic field. However, the magnetic dipolar interaction between SKBs, which influences the chirality of some SKBs and further modifies the final statistical results, cannot be neglected. If the magnetic field is applied parallel to the thickness gradient direction, or along the y direction, different features appear: the chirality reverses randomly and no special chirality is preferred [Fig. 5(c)]. For comparison, the same operation is simulated in another flat slab (Fig. S8 within the Supplemental Material [31]). Unlike the wedge-shaped thin

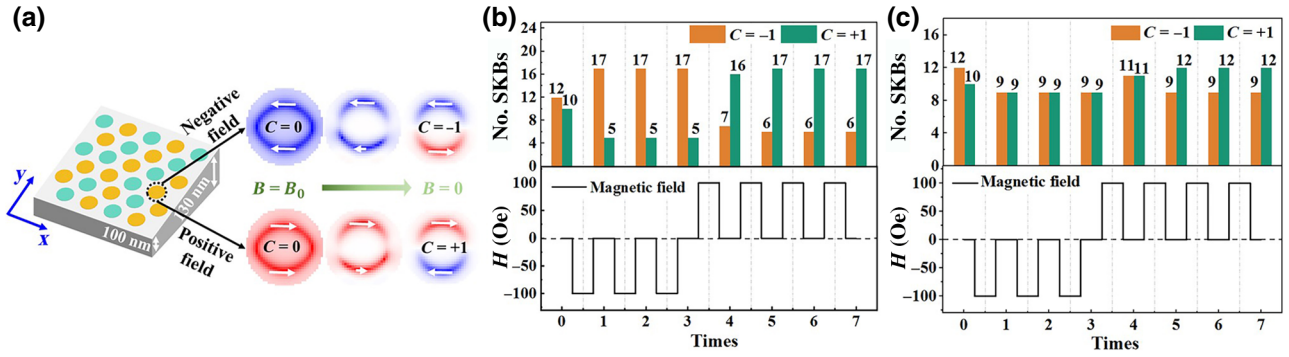

FIG. 5. Analyses of chirality reversal calculations with external in-plane magnetic fields. (a) Sketch of the field-dependent evolution for skyrmion bubbles ($C = \pm 1$) and achiral bubbles ($C = 0$). B_0 is a critical magnetic field where a single skyrmion bubble transforms into achiral bubble. The magnetic field is applied along the $-x$ and $-y$ directions. The white arrows represent the direction of in-plane magnetization. The surface size of the wedgelike slab is 1000×1000 nm^2 and the thickness changes between 100 and 130 nm. (b) The reversal statistics for the in-plane magnetic field perpendicular to the thickness gradient and (c) for the magnetic field along the gradient direction.

plate, the $C = \pm 1$ SKBs maintain almost same quantity during modulation of the in-plane magnetic field. These simulations demonstrate that the thickness variation in the materials should be an additional freedom to manipulate the chirality of the SKBs, if combined with coding of the in-plane magnetic field, which provides an alternative route to device applications for magnetic skyrmions.

IV. SUMMARY

Spin chirality reversal of SKBs is directly observed in $(Mn_{1-x}Ni_x)_{65}Ga_{35}$ centrosymmetric magnets by using LTEM at room temperature. Remarkably, the in-plane magnetic field can activate the quantity of SKB reversal. Micromagnetic simulations demonstrate that the collective behavior of spin chirality can be strongly affected by the sample thickness, when the direction of the magnetic field is inversed. The static energy difference between the thinner and thicker parts within a bubble, associated with coupling among the bubbles, results in the reversal of chirality. These findings provide a basic mechanism for manipulating the spin chirality of SKBs in centrosymmetric magnets and may also lead to a promising application in nonvolatile spintronic devices with reduced power dissipation.

To date, the key operation of skyrmion racetrack memory is to move skyrmions with electrical currents to perform read or write functions [36]. Although promising for technological application, current-driven skyrmion motion is intrinsically collective and feasible only in conductive materials and is accompanied by undesired heating effects [37]. Here, we experimentally demonstrate that a noncontacting in-plane magnetic field can be used to manipulate zero-field skyrmion bubbles efficiently. In this way, the skyrmion material is no longer detrimentally perturbed by the source of manipulation. The required energy is also significantly reduced compared to that of the current-driven scheme, and it can be applied to all skyrmion-hosting materials, regardless of their conductivity. Such applications can also control their local creation and annihilation: the existence of a skyrmion bubble is thereby interpreted as "1" and "−1" and its absence as a "0" bit, which can be further induced by the in-plane magnetic field.

Moreover, as devices are surface-dominated, the influence of surfaces on the spin structure is a key question. While a wide range of methods exist for studying 2D skyrmion bubbles, comprehensive knowledge of 3D magnetic dynamics remains elusive. Here, combined with micromagnetic simulations, we reveal a nonuniform and nontrivial dynamic transition on the surfaces and center of the SKBs and achiral bubbles. Importantly, we report asymmetric chirality manipulation, which can be further explained from the perspective of static energy. Nevertheless, static energy effects on the SKB chirality cannot be accurately described by theory at present. We hope our work will lead to more experimental and theoretical studies in this field.

ACKNOWLEDGMENTS

This work is supported by the National Key R&D Program of China (Grants No. 2017YFA0303202 and No. 2017YFA0206303), the National Natural Science Foundation of China (Grants No. 11604148 and No. 11874410), and the Key Research Program of the Chinese Academy of Sciences (Grant No. KJZD-SW-M01).

[1] A. Tonomura, X. Yu, K. Yanagisawa, T. Matsuda, Y. Onose, N. Kanazawa, H. S. Park, and Y. Tokura, Real-space observation of skyrmion lattice in helimagnet MnSi thin samples, Nano Lett. **12**, 1673 (2012).

[2] A. Neubauer, C. Pfleiderer, B. Binz, A. Rosch, R. Ritz, P. G. Niklowitz, and P. Boni, Topological Hall Effect in the A Phase of MnSi, Phys. Rev. Lett. **102**, 186602 (2009).

[3] S. Mühlbauer, B. Binz, F. Jonietz, C. Pfleiderer, A. Rosch, A. Neubauer, R. Georgii, and P. Böni, Skyrmion lattice in a chiral magnet, Science **323**, 915 (2009).

[4] H. Wilhelm, M. Baenitz, M. Schmidt, U. K. Rößler, A. A. Leonov, and A. N. Bogdanov, Precursor Phenomena at the Magnetic Ordering of the Cubic Helimagnet FeGe, Phys. Rev. Lett. **107**, 127203 (2011).

[5] X. Z. Yu, N. Kanazawa, Y. Onose, K. Kimoto, W. Z. Zhang, S. Ishiwata, Y. Matsui, and Y. Tokura, Near room-temperature formation of a skyrmion crystal in thin-films of the helimagnet FeGe, Nat. Mater. **10**, 106 (2010).

[6] X. Z. Yu, Y. Onose, N. Kanazawa, J. H. Park, J. H. Han, Y. Matsui, N. Nagaosa, and Y. Tokura, Real-space observation of a two-dimensional skyrmion crystal, Nature **465**, 901 (2010).

[7] T. Adams, A. Chacon, M. Wagner, A. Bauer, G. Brandl, B. Pedersen, H. Berger, P. Lemmens, and C. Pfleiderer, Long-Wavelength Helimagnetic Order and Skyrmion Lattice Phase in Cu_2OSeO_3, Phys. Rev. Lett. **108**, 237204 (2012).

[8] S. Seki, X. Z. Yu, S. Ishiwata, and Y. Tokura, Observation of skyrmions in a multiferroic material, Science **336**, 198 (2012).

[9] S. Seki, S. Ishiwata, and Y. Tokura, Magnetoelectric nature of skyrmions in a chiral magnetic insulator Cu_2OSeO_3, Phys. Rev. B **86**, 060403 (2012).

[10] A. K. Nayak, V. Kumar, T. Ma, P. Werner, E. Pippel, R. Sahoo, F. Damay, U. K. Rößler, C. Felser, and S. S. P. Parkin, Magnetic antiskyrmions above room temperature in tetragonal Heusler materials, Nature **548**, 561 (2017).

[11] Y. Onose, Y. Okamura, S. Seki, S. Ishiwata, and Y. Tokura, Observation of Magnetic Excitations of Skyrmion Crystal in a Helimagnetic Insulator Cu_2OSeO_3, Phys. Rev. Lett. **109**, 037603 (2012).

[12] H. Oike, A. Kikkawa, N. Kanazawa, Y. Taguchi, M. Kawasaki, Y. Tokura, and F. Kagawa, Interplay between topological and thermodynamic stability in a metastable magnetic skyrmion lattice, Nat. Phys. **12**, 62 (2015).

[13] K. Shibata, J. Iwasaki, N. Kanazawa, S. Aizawa, T. Tanigaki, M. Shirai, T. Nakajima, M. Kubota, M. Kawasaki, H. S. Park, D. Shindo, N. Nagaosa, and Y. Tokura, Large anisotropic deformation of skyrmions in strained crystal, Nat. Nanotechnol. **10**, 589 (2015).

[14] T. Srivastava, M. Schott, R. Juge, V. Křižáková, M. Belmeguenai, Y. Roussigné, A. Bernand-Mantel, L. Ranno, S. Pizzini, S.-M. Chérif, A. Stashkevich, S. Auffret, O. Boulle, G. Gaudin, M. Chshiev, C. Baraduc, and H. Béa, Large-voltage tuning of dzyaloshinskii–moriya interactions: A route toward dynamic control of skyrmion chirality, Nano Lett. **18**, 4871 (2018).

[15] M. Schott, A. Bernand-Mantel, L. Ranno, S. Pizzini, J. Vogel, H. Béa, C. Baraduc, S. Auffret, G. Gaudin, and D. Givord, The skyrmion switch: Turning magnetic skyrmion bubbles on and off with an electric field, Nano Lett. **17**, 3006 (2017).

[16] K. Shibata, X. Z. Yu, T. Hara, D. Morikawa, N. Kanazawa, K. Kimoto, S. Ishiwata, Y. Matsui, and Y. Tokura, Towards control of the size and helicity of skyrmions in helimagnetic alloys by spin–orbit coupling, Nat. Nanotechnol. **8**, 723 (2013).

[17] Z.-A. Li, F. Zheng, A. H. Tavabi, J. Caron, C. Jin, H. Du, A. Kovács, M. Tian, M. Farle, and R. E. Dunin-Borkowski, Magnetic skyrmion formation at lattice defects and grain boundaries studied by quantitative off-axis electron holography, Nano Lett. **17**, 1395 (2017).

[18] S. Zhang, J. Zhang, Y. Wen, E. M. Chudnovsky, and X. Zhang, Determination of chirality and density control of Néel-type skyrmions with in-plane magnetic field, Commun. Phys. **1**, 36 (2018).

[19] W. H. Wang, Y. Zhang, G. Z. Xu, L. C. Peng, B. Ding, Y. Wang, Z. P. Hou, X. M. Zhang, X. Y. Li, E. K. Liu, S. H. Wang, J. W. Cai, F. W. Wang, J. Q. Li, F. X. Hu, G. H. Wu, B. G. Shen, and X.-X. Zhang, A centrosymmetric hexagonal magnet with superstable biskyrmion magnetic nanodomains in a wide temperature range of 100–340 K, Adv. Mater. **28**, 6887 (2016).

[20] C. Phatak, O. Heinonen, M. De Graef, and A. Petford-Long, Nanoscale skyrmions in a nonchiral metallic multiferroic: Ni_2MnGa, Nano Lett. **16**, 4141 (2016).

[21] Z. Hou, W. Ren, B. Ding, G. Xu, Y. Wang, B. Yang, Q. Zhang, Y. Zhang, E. Liu, F. Xu, W. Wang, G. Wu, X. Zhang, B. Shen, and Z. Zhang, Observation of various and spontaneous magnetic skyrmionic bubbles at room temperature in a frustrated kagome magnet with uniaxial magnetic anisotropy, Adv. Mater. **29**, 1701144 (2017).

[22] X. Yu, M. Mostovoy, Y. Tokunaga, W. Zhang, K. Kimoto, Y. Matsui, Y. Kaneko, N. Nagaosa, and Y. Tokura, Magnetic stripes and skyrmions with helicity reversals, Proc. Natl Acad. Sci. U.S.A. **109**, 8856 (2012).

[23] N. Nagaosa and Y. Tokura, Topological properties and dynamics of magnetic skyrmions, Nat. Nanotechnol. **8**, 899 (2013).

[24] X. Zhang, J. Xia, Y. Zhou, X. Liu, H. Zhang, and M. Ezawa, Skyrmion dynamics in a frustrated ferromagnetic film and current-induced helicity locking-unlocking transition, Nat. Commun. **8**, 1717 (2017).

[25] X. Z. Yu, K. Shibata, W. Koshibae, Y. Tokunaga, Y. Kaneko, T. Nagai, K. Kimoto, Y. Taguchi, N. Nagaosa, and Y. Tokura, Thermally activated helicity reversals of skyrmions, Phys. Rev. B **93**, 134417 (2016).

[26] X. Yu, Y. Tokunaga, Y. Taguchi, and Y. Tokura, Variation of topology in magnetic bubbles in a colossal magnetoresistive manganite, Adv. Mater. **29**, 1603958 (2017).

[27] L. Peng, Y. Zhang, W. Wang, M. He, L. Li, B. Ding, J. Li, Y. Sun, X. G. Zhang, J. Cai, S. Wang, G. Wu, and B. Shen, Real-space observation of nonvolatile zero-field biskyrmion lattice generation in MnNiGa magnet, Nano Lett. **17**, 7075 (2017).

[28] G. Asti and F. Bolzoni, Singular point detection of discontinuous magnetization processes, J. Appl. Phys. **58**, 1924 (1985).

[29] G. Asti and S. Rinaldi, Singular points in the magnetization curve of a polycrystalline ferromagnet, J. Appl. Phys. **45**, 3600 (1974).

[30] G. Asti and S. Rinaldi, Nonanaliticity of the Magnetization Curve: Application to the Measurement of Anisotropy in Polycrystalline Samples, Phys. Rev. Lett. **28**, 1584 (1972).

[31] See the Supplemental Material at http://link.aps.org/supplemental/10.1103/PhysRevApplied.12.054060 for details of experiments and simulations and a video of field cooling manipulation.

[32] K. Ishizuka and B. Allman, Phase measurement of atomic resolution image using transport of intensity equation, J. Electron. Microsc. **54**, 191 (2005).

[33] M. J. Donahue and D. G. Porter, Object Oriented Micromagnetic Framework User's Guide Version 1.0 NISTIR 6376, National Institute of Standards and Technology (Gaithersburg, MD, USA, 1999).

[34] J. Cui, Y. Yao, X. Shen, Y. G. Wang, and R. C. Yu, Artifacts in magnetic spirals retrieved by transport of intensity equation (TIE), J Magn Magn Mater. **454**, 304 (2018).

[35] B. Ding, H. Li, X. Li, Y. Wang, Z. Hou, G. Xu, E. Liu, G. Wu, F. Wang, and W. Wang, Crystal-orientation dependence of magnetic domain structures in the skyrmion-hosting magnets MnNiGa, APL Mater. **6**, 076101 (2018).

[36] S. S. P. Parkin, M. Hayashi, and L. Thomas, Magnetic domain-wall racetrack memory, Science **320**, 190 (2008).

[37] X. Zhao, S. Wang, C. Wang, and R. Che, Thermal effects on current-related skyrmion formation in a nanobelt, Appl. Phys. Lett. **112**, 212403 (2018).